International Journal of Concrete Structures and Materials

RESEARCH Open Access

Numerical Implementation of an Additive Strain Model for the Damage Simulation of Fatigue-Loaded Concrete

Dennis Birkner[1] and Steffen Marx[2*]

Abstract

Investigating the fatigue behavior of concrete structures from wind turbine towers is associated with major challenges due to the high number of occurring load cycles and large cross-sectional dimensions. Thus, only few studies have been carried out on concrete structures subjected to cyclic bending loads. Numerical simulations, in contrast, enable fast investigations of many parameter variations. There are many material models available for different applications, yet they quickly become very complex and require time-consuming calibration of input parameters in structural tests. A model for simulating macroscopic damage processes in fatigue-loaded compressed concrete cross sections, which can be calibrated using standard cylinder tests, does not yet exist. The present work aims to close this gap and implements an additive strain model to simulate the strain and damage development of concrete subjected to fatigue bending loads. Therefore, experimental investigations were designed and carried out. Static and cyclic tests on concrete cylinders yielded the input parameters for the material model. A strain model was implemented in ANSYS Mechanical. The numerical implementation was validated using fatigue tests on large prestressed beams in a resonance-based testing facility. The beam specimens mostly failed due to fatigue in the compression zone. The numerical model confirmed the effects observed in the beam tests and was able to simulate the most damaged regions very well. Moreover, stress redistribution to less loaded regions as a result of relief of the damaged regions was detected. This confirmed the positive effect of stress redistributions on the fatigue life of the structures.

Keywords Concrete, Damage, Fatigue, FEM, Stress redistribution, ANSYS

1 Introduction

One way to reduce global CO_2 emissions is to use more renewable energy sources. Wind energy in particular plays an important role in this regard. To increase the energy yield from wind energy, more and higher turbines are constantly being built (Klein & Marx, 2021). In the onshore sector, these are mostly hybrid towers, of which two-thirds consist of stacked and prestressed concrete ring segments with dry joints and one-third of a steel tower (Bögl et al., 2013). As the hub heights increase, the structures become increasingly slender and the material utilization steadily grows (Fürll et al., 2024). As a result of the cyclical effects from the wind, fatigue verification is becoming increasingly important in design. Extensive experimental investigations on large-scale specimens are required for more detailed research into the structural behavior of concrete subjected to fatigue loading (Schramm et al., 2024). These exhibit high numbers of cycles to failure due to changes in stiffness and stress redistributions (Monteiro et al., 2024) and can, therefore, take a very long time (Becks et al., 2023; Birkner & Marx, 2021). As a consequence, only a few research results exist in

Journal information: ISSN 1976-0485 / eISSN 2234-1315.

*Correspondence:
Steffen Marx
steffen.marx1@tu-dresden.de
[1] Ramboll Deutschland GmbH, Lister Str. 9, 30163 Hannover, Germany
[2] Institute of Concrete Structures, Dresden University of Technology, 01062 Dresden, Germany

this field to date. In addition, the current design regulations still have very high safety margins, which lead to very conservative designs (Baktheer et al., 2024; Birkner & Marx, 2022). One way to reduce this high necessary effort is by simulation with numerical models. Material models of classic plasticity or damage theory are often used for the simulation of concrete under static loading (Birkner et al., 2023; Makhlouf et al., 2024; Wu et al., 2022). However, in the case of fatigue loading, there are usually stresses that lie below the material strength and still lead to cracking and damage processes in the material (Becks et al., 2022). The models must, therefore, be extended to be able to account for these processes (Mai et al., 2012).

In recent decades, a large number of such constitutive models have been developed to describe the material behavior of concrete at the macro- and mesolevel. According to Baktheer and Chudoba (2019), these can usually be divided into two groups. The models of one group follow the approach of describing the fatigue behavior as a function of load cycles, e.g., (Grünberg et al., 2014; Pfanner, 2003). Models that are based on continuum damage mechanics and formulate fatigue damage as a function of strain can be assigned to the second group, e.g., (Abhijith & Atul Narayan, 2023; Alliche, 2004; Desmorat et al., 2007; Kindrachuk et al., 2015). Microplane models (Baktheer et al., 2021; Betz et al., 2023; Kirane & Bažant, 2015) or models using the phase field method (Baktheer et al., 2024c; Krüger et al., 2024) have also been developed to simulate the fatigue behavior of concrete. Newer models also use machine-based learning methods like the Gradient boosting regression tree (GBRT) to predict the fatigue behavior based on results from literature (Liang et al., 2023).

Only a few studies have investigated the simulation of concrete beams so far. The microplane model developed in Kirane and Bažant (2015) was applied to notched beams failing due to tension cracks and can be used to predict the crack growth. To simulate the fatigue behaviour of presetressed reinforced beams, a theoretical model was developed in Carpinteri et al. (2005). It is valid for failure due to cracking in the tensile area, slip between reinforcement and concrete, yielding of the reinforcement and crushing of concrete in the compression zone. However, no information about the possibility to simulate stress redistributions is given. This was investigated in Zanuy et al. (2009). A cycle-dependent model which can account for the changes of stiffness distribution due to fatigue damage is proposed and compared to a test series on reinforced concrete beams. It is found that the failure type of the beams depends on the sectional capacity for redistribution of stresses. Another example for the simulation of stress redistributions in prestressed concrete beams failing due to compression can be found in Baktheer et al. (2024). The implemented microplane fatigue model is able to simulate these processes well and additionally allows to assess the dissipated energy during the fatigue life because of its thermodynamic nature.

In general, when choosing a material model, a compromise must always be made between accuracy and calculation effort. There are a large number of models in the literature that are suitable for the numerical simulation of concrete. However, they each pursue different objectives and are better at simulating certain effects than others. In addition, they usually require complex calibration on component tests. A model for simulating the macroscopic damage processes in concrete cross sections under compressive fatigue loading, like in structural elements of wind turbines, which can be calibrated using conventional cylinder tests, does not yet exist and will be presented in this work. For this purpose, the mechanically based strain model from von der Haar and Marx (2018) is extended and implemented into the finite element software ANSYS Mechanical.

2 Summary of the Additive Strain Model

The most important elements of the model are summarized here; for more detailed information, please refer to the original source in von der Haar and Marx (2018). In the model, concrete strains due to fatigue loading consist of four separate components—an elastic strain component ε_{el}, a load cycle-dependent plastic strain component ε_{d}, a time-dependent viscous strain component ε_{cr} and a temperature strain component ε_{t}. Shrinkage deformations are neglected in the model due to comparatively short durations of fatigue tests compared to the service life of structures. The total strain ε_{fat}, which is measured on specimens during fatigue loading, can be described by Eq. (1). The first three strain components are compressions and the strain values are, therefore, defined to be negative. The strains resulting from specimen heating are defined to be positive, because they lead to an expansion of the specimens, and, therefore, reduce the strain measured in fatigue tests. The strain components are assumed to be independent of each other, making this an additive strain model:

$$|\varepsilon_{fat}| = |\varepsilon_{el}| + |\varepsilon_{d}| + |\varepsilon_{cr}| - |\varepsilon_{t}| \tag{1}$$

The elastic strain component is described by Hooke's law according to Eq. (2) and corresponds to reversible deformations between the maximum stress level σ_{max} and the relieved state. The curved shape of the loading and unloading branches is neglected for this model. The secant modulus $E_c(N)$ decreases with increasing number of load cycles depending on the stress and represents the degradation of the material stiffness:

$$\varepsilon_{el} = \varepsilon_{max} = \frac{\sigma_{max}}{E_c(N)} \quad (2)$$

Irreversible deformations that occur as a result of material disruption are taken into account via the plastic strain component. The magnitude of this strain cannot be measured directly in experiments, but must be calculated subtracting the other strain components from the measured total strain ε_{fat} according to Eq. (1). In von der Haar and Marx (2018), this was evaluated as part of the investigations. A linear relationship was found between the calculated plastic strain component and the logarithmized number of cycles to failure of the specimens.

The deformations from concrete heating as a result of fatigue loading are taken into account via the thermal strain component. During each load cycle, part of the energy induced is converted into thermal energy. This corresponds to the hysteresis area between an unloading and reloading path in the stress–strain diagram. The specimen heating, therefore, depends on the stress amplitude, loading frequency, thermal conductivity and convection and heat transfer conditions on the specimen surface. The thermal strains ε_t are calculated using Eq. (3) with the coefficient of thermal expansion of concrete α_T and the mean temperature change ΔT:

$$\varepsilon_t = \alpha_T \cdot \Delta T \quad (3)$$

However, heating of concrete as a result of fatigue loading mainly occurs in experiments, e.g., (Bode & Marx, 2019; Deutscher et al., 2020), as these are carried out at loading frequencies that are significantly higher than fatigue loads actually occurring on components to reduce the time required. This strain component must, therefore, be taken into account when evaluating fatigue tests.

All visco-elastic strains resulting from time-dependent creep behavior of concrete are taken into account in the viscous strain component. Visco-plastic deformations from permanent loading are taken into account by the plastic strain component. To determine the viscous strain component, it is assumed that for each fatigue stress level there is a static equivalent stress that causes the same creep strains. This equivalent stress is referred to as creep-relevant stress level. With this parameter, the viscous strain in concrete subjected to fatigue loading can be determined. The calculation of the creep-relevant stress level was developed in von der Haar and Marx (2018). It was shown that the creep-relevant stress level and the mean stress level of the cyclic loading are identical if the maximum stress level of the cyclic loading is below the linearity limit of concrete creep. Otherwise, the magnitude of the creep-relevant stress level is between the medium stress level and the maximum stress level. These observations were also confirmed in recent studies (Kern et al., 2024).

3 Experimental Investigations on Prestressed Concrete Beams

Experimental fatigue tests were carried out on eight large-scale prestressed concrete beams. Two different types of concrete and two load levels were investigated as a basis for validating the numerical model. The beams were tested in a resonance-based testing facility. Table 1 gives an overview of the concrete compositions and Table 4 shows the targeted load levels for each beam specimen. Two tests were planned for each combination of concrete strength and load level.

In addition, 43 fatigue tests on cylindrical specimens with a diameter $D = 100$ mm and height $H = 300$ mm were carried out in a servo-hydraulic testing machine in a force-controlled regime up to failure. During the tests, the machine force, the machine path and the specimen deformations in the longitudinal direction were continuously recorded by four laser distance sensors, which were arranged around the specimen circumference every 90 degrees. These tests were evaluated with respect to the specimen stiffness over the relative fatigue life which is used as input for the numerical implementation, as described in Sect. 4.1. A detailed evaluation can be found in Birkner et al. (2024).

The static system of the beam tests was a four-point bending setup. The beam specimens had an inverted T-shaped cross section, were supported on steel rolls at both ends and constructively restrained against longitudinal and transversal movements. Two steel traverses were placed in the middle of the beam with 1.4 m distance to each other and were used to apply the static loads via vertical threaded rods. These were prestressed by springs anchored in a cellar below the test setup. The vertical spring prestressing was used to adjust the stress level in the beams. Extra weights on the traverses were added to adjust the natural frequency of the system. Longitudinal prestressing using unbonded threaded rods prevented tensile stresses at the bottom of the concrete beams. Therefore, the tendons were located eccentrically below the centre of mass of the beams. In combination

Table 1 Concrete compositions used in the test series

Description	C40	C80
Cement	CEM II/A-LL 42.5 N	CEM I 52.5 R
Aggregate 2/8	Crushed Limestone	Quartz gravel
Aggregate 8/16	Crushed Limestone	Crushed Limestone
w/c ratio	0.50	0.47

with the dead weight of the specimens, these loads represented the static loads during the test.

The dynamic loads were generated by four imbalance motors. These were mounted pairwise on the two traverses and were operated near the first natural bending frequency of the beams and caused them to resonate. The dynamic magnification of the load allowed the generation of the required large stress at the specimen edges with comparatively low imbalance forces. The dynamic forces were held constant during the tests by a regulation software. With this setup high excitation frequencies of up to 25 Hz could be realised and allowed to reach much higher numbers of load cycles in the same test duration with much less energy consumption compared to a conventional hydraulic testing facility. The principle of the resonance-based testing facility is described thoroughly in Schneider et al. (2018). A more detailed description of the specimens and the test setup can be found in Birkner et al. (2024). In the beam tests a minimum stress level of $S_{min} = \sigma_{min}/f_{cm} = 0.05$ and maximum stress levels $S_{max} = \sigma_{max}/f_{cm} = 0.75$ and 0.65 at the top of the beams in midspan were targeted, as shown in Fig. 1.

The support forces were measured with force sensors and used as control parameter for the dynamic load. Calibrated strain gages in full bridge circuit measured the forces in the vertical threaded rods and ring force sensors the forces in the longitudinal threaded rods. In mid span, strain gages were applied to measure concrete strains and thermocouples for the surface temperature, see Fig. 2. Changes in the strains over the test duration allowed to draw conclusions about the deformation of the specimens and about any occurring damage. Due to the high frequent loading the specimens heated up which led to additional thermal strains. The temperatures were measured along the web height to quantify them. Fig. 3 shows the significant temperature changes for all sensors over the relative fatigue life of beam C40–4 exemplarily.

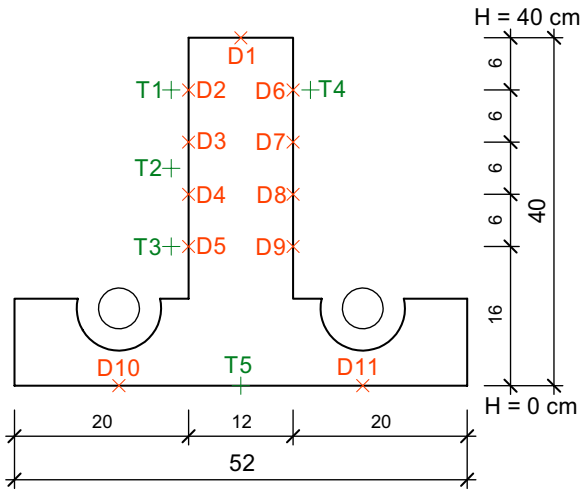

Fig. 2 Location of the strain gages (D1 to D11) and temperature sensors (T1 to T5) at the beams

4 Numerical Implementation of the Additive Strain Model

4.1 Elastic Strain Component

In the numerical model the elastic strains are calculated directly from the external loads at the maximum and minimum stress levels using Hooke's law. They only depend on the modulus of elasticity of the individual elements. The latter, however, is only identical for all elements at the beginning of loading. The successive stiffness degradation during fatigue loading is represented by an elementwise decrease in the modulus of elasticity. In the numerical model, different combinations of maximum and minimum stress levels occur at different elements under a certain external load. It would require an unrealistically large experimental and

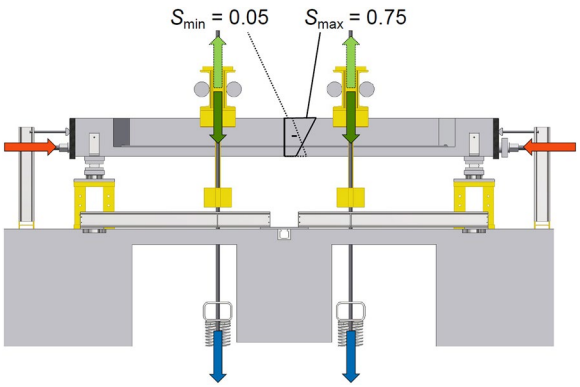

Fig. 1 Schematic illustration of the loads and stresses at the maximum (dark green, solid lines) and the minimum stress level (light green, dashed lines): longitudinal prestressing (red), vertical spring prestressing (blue) and cyclic imbalance load (green)

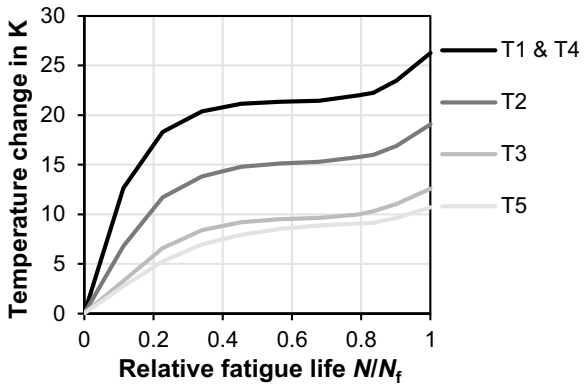

Fig. 3 Exemplary temperature curves for sensors T1 to T5 of beam C40–4

time effort to determine stiffness functions for all possible stress levels. Therefore, only mean stiffness curves from fatigue tests on concrete cylinders with the same stress levels as the beams were considered. The later evaluation confirmed that this approach is suitable and can describe the stiffness degradation in the numerical model with phenomenological accuracy.

As the cylinders of the two investigated concretes showed different stiffness curves and residual stiffnesses, an approximation function was determined for each concrete. This function $D(\nu)$ maps three phases $D^{\mathrm{I}}(\nu)$ to $D^{\mathrm{III}}(\nu)$ in analogy to the characteristic material behavior of concrete under fatigue loading. The first and last phases are each described using an exponential approach, the second phase using a linear function. The damage has a value of 0 at the beginning and increases with successive test duration up to a maximum value of 1. The functions are described by Eqs. (4)–(12), Table 2 contains the associated parameters which were obtained by a best-fit analysis to match the experimental data, as shown in Fig. 4:

$$D^{\mathrm{I}}(\nu) = a_1 \cdot \nu^{b_1} \tag{4}$$

$$D^{\mathrm{II}}(\nu) = D^{\mathrm{I/II}} + \overline{D}^{\mathrm{II}} \cdot (\nu - \nu^{\mathrm{I/II}}) \tag{5}$$

$$D^{\mathrm{III}}(\nu) = 1 - a_3 \cdot (1 - \nu)^{b_3} \tag{6}$$

$$\overline{D}^{\mathrm{II}} = \frac{D^{\mathrm{II/III}} - D^{\mathrm{I/II}}}{\nu^{\mathrm{II/III}} - \nu^{\mathrm{I/II}}} \tag{7}$$

$$\Delta D^{\mathrm{III}} = 1 - D^{\mathrm{II/III}} \tag{8}$$

$$a_1 = \frac{D^{\mathrm{I/II}}}{\nu^{\mathrm{I/II}b_1}} \tag{9}$$

$$b_1 = \frac{\overline{D}^{\mathrm{II}} \cdot \nu^{\mathrm{I/II}}}{D^{\mathrm{I/II}}} \tag{10}$$

Table 2 Parameters for the phase transitions of the approximation functions for damage

Parameter	C40	C80
$\nu^{\mathrm{I/II}}$	0.25	0.25
$\nu^{\mathrm{II/III}}$	0.75	0.75
$D^{\mathrm{I/II}}$	0.42	0.26
$D^{\mathrm{II/III}}$	0.59	0.45

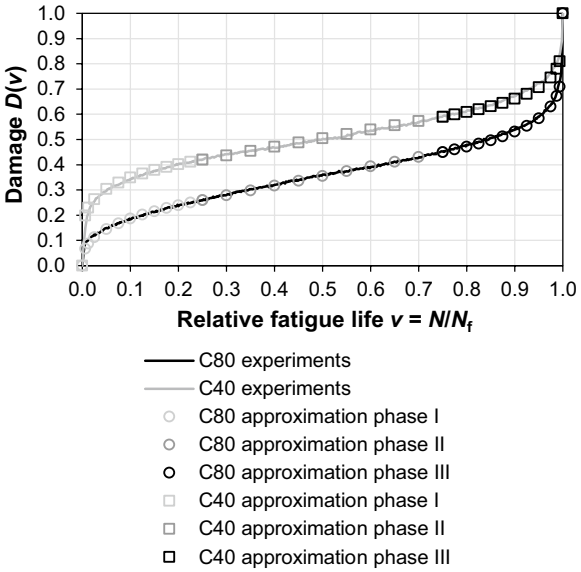

Fig. 4 Approximation function compared to the mean damage curves of the experiments

$$a_3 = \frac{\Delta D^{\mathrm{III}}}{\left(1 - \nu^{\mathrm{II/III}}\right)^{b_3}} \tag{11}$$

$$b_3 = \frac{\overline{D}^{\mathrm{II}} \cdot \left(1 - \nu^{\mathrm{II/III}}\right)}{\Delta D^{\mathrm{III}}} \tag{12}$$

Fig. 4 compares the resulting damage functions with the mean damage curves from the experiments and clearly shows the good agreement between them. These functions can be used in the numerical model to calculate the damage of an element as a function of the relative fatigue life. To maintain numerical stability, a residual stiffness is applied when an element reaches complete failure, which corresponds to the stiffness in the last complete load cycle in the fatigue test. This is achieved by converting the damage $D(\nu)$ into a modified damage $D^*(\nu)$ using Eq. (13). The parameter $E_{\mathrm{c,f,mean}}$ is the mean value of all residual stiffness values $E_{\mathrm{c,f},i}$ and $E_{\mathrm{c,0,mean}}$ the mean value of the initial stiffness values of the tested cylinders of the same concrete strength. The relative stiffness function $\eta(\nu)$ is then obtained using Eq. (14). It can be used to calculate the relative stiffness for each element at each point of fatigue life ν. The element stiffness is then adjusted in the model by multiplying it with the initial value of the modulus of elasticity. Fig. 5 shows the resulting relative stiffness functions.

$$D^*(\nu) = \left(1 - \frac{E_{\mathrm{c,f,mean}}}{E_{\mathrm{c,0,mean}}}\right) \cdot D(\nu) \tag{13}$$

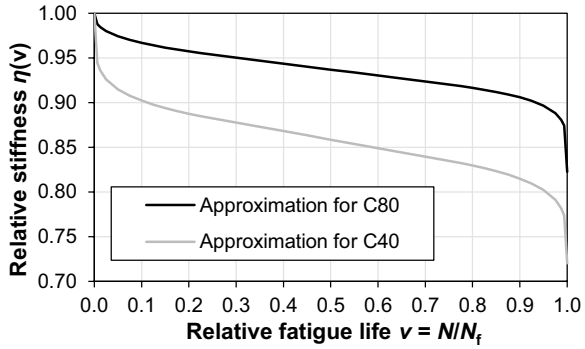

Fig. 5 Relative stiffness functions over the relative fatigue life

$$\eta(\nu) = 1 - D^*(\nu) \tag{14}$$

The relative fatigue life ν indicates the proportion of the maximum endurable load cycles that has already been accumulated for each element. It starts at 0 at the beginning of the calculation and is increased incrementally by the value $\Delta\nu$ with each load collective until complete damage of the element is reached and ν becomes 1. The increment size depends on the number of load cycles ΔN_i, which is applied in the current load collective i, and the maximum and minimum stress of the element. The principal stresses σ_{I}, σ_{II} and σ_{III} are used to account for arbitrary load conditions. With these, the number of cycles to failure $N_{\mathrm{f},i}^{k}$ according to *fib* Model Code 2010 (fib, 2013) is calculated separately for each principal axis k and then the matrix $\boldsymbol{\Delta\nu}_i^{\mathrm{PS}}$ of the relative fatigue life increment in the principal stress space (PS) is formulated according to the following equation:

$$\boldsymbol{\Delta\nu}_i^{\mathrm{PS}} = \begin{bmatrix} \Delta\nu_{\mathrm{I}} & 0 & 0 \\ 0 & \Delta\nu_{\mathrm{II}} & 0 \\ 0 & 0 & \Delta\nu_{\mathrm{III}} \end{bmatrix} = \begin{bmatrix} \frac{\Delta N_i}{N_{\mathrm{f},i}^{\mathrm{I}}} & 0 & 0 \\ 0 & \frac{\Delta N_i}{N_{\mathrm{f},i}^{\mathrm{II}}} & 0 \\ 0 & 0 & \frac{\Delta N_i}{N_{\mathrm{f},i}^{\mathrm{III}}} \end{bmatrix} \tag{15}$$

Since different stress distributions occur in the various load collectives, the principal directions of the collectives also differ from each other and the relative fatigue life increments cannot be cumulated. The global xyz-coordinate system is selected as a common basis for this purpose. Then, a base transformation from the principal stress system to the global coordinate system is carried out according to Eq. (16). This is achieved using the transformation matrix $\boldsymbol{T}_i^{\mathrm{PS}\to xyz}$ according to Eq. (17), which contains the eigenvectors $e_{k,j}$ of the principal directions in the global coordinate system j. The matrix $\boldsymbol{\Delta\nu}_i^{\mathrm{PS}}$ is transformed into the global coordinate system using the base transformation, resulting in the matrix $\boldsymbol{\Delta\nu}_i^{xyz}$. It contains the relative fatigue life increments in the global coordinate system, see Eq. (18):

$$\boldsymbol{\Delta\nu}_i^{xyz} = \boldsymbol{T}_i^{\mathrm{PS}\to xyz}\,\boldsymbol{\Delta\nu}_i^{\mathrm{PS}}\,\boldsymbol{T}_i^{\mathrm{PS}\to xyz\,\mathrm{T}} \tag{16}$$

$$\boldsymbol{T}_i^{\mathrm{PS}\to xyz} = \begin{bmatrix} e_{\mathrm{I},x} & e_{\mathrm{II},x} & e_{\mathrm{III},x} \\ e_{\mathrm{I},y} & e_{\mathrm{II},y} & e_{\mathrm{III},y} \\ e_{\mathrm{I},z} & e_{\mathrm{II},z} & e_{\mathrm{III},z} \end{bmatrix} \tag{17}$$

$$\boldsymbol{\Delta\nu}_i^{xyz} = \begin{bmatrix} \Delta\nu_{xx} & \Delta\nu_{xy} & \Delta\nu_{xz} \\ \Delta\nu_{xy} & \Delta\nu_{yy} & \Delta\nu_{yz} \\ \Delta\nu_{xz} & \Delta\nu_{yz} & \Delta\nu_{zz} \end{bmatrix} \tag{18}$$

To calculate the isotropic stiffness degradation of the elements, the matrix is converted into a scalar parameter $\Delta\nu_{\mathrm{res},i}$ according to Eq. (19). This is interpreted as the size of the fatigue life increment. This resulting increment is then added to the value of the relative fatigue life of the previous iteration step ν_{i-1} and results in the current relative fatigue life ν_i of the element according to Eq. (20). With this value, the stiffness can be determined using the previously presented relative stiffness function $\eta(\nu)$:

$$\Delta\nu_{\mathrm{res},i} = \sqrt{\Delta\nu_{xx}{}^2 + \Delta\nu_{yy}{}^2 + \Delta\nu_{zz}{}^2 + 2\cdot\Delta\nu_{xy}{}^2 + 2\cdot\Delta\nu_{xz}{}^2 + 2\cdot\Delta\nu_{yz}{}^2} \le 1 \tag{19}$$

$$\nu_i = \nu_{i-1} + \Delta\nu_{\mathrm{res},i} \tag{20}$$

With this modification into a scalar parameter, the stiffness development can only be considered isotropically. Since fatigue loads usually have a predominant direction in reality, this simplification is considered appropriate.

4.2 Viscous Strain Component

The viscous strains are determined using the creep coefficient $\varphi(t_i, t_0)$ according to *fib* Model Code 2010 (fib, 2013). In contrast to the creep function of the Model Code, the creep-relevant stress $\sigma_{\mathrm{cr,eq}}$ is used instead of the actual stress. It is determined for each element based on the current maximum and minimum stress of the current load spectrum according to von der Haar and Marx (2018):

$$\varepsilon_{\mathrm{cr}}(t_i, t_0) = \frac{\sigma_{\mathrm{cr,eq}}}{E_i} \cdot \varphi(t_i, t_0) \tag{21}$$

The viscous strain of the element is then calculated using the creep-relevant stress according to Eq. (21).

This equation describes the creep strain $\varepsilon_{\mathrm{cr}}$ that an element exhibits after a period of time $t_i - t_0$ when subjected to an applied constant stress over the entire loading period. Due to material degradation, however, there

will be stiffness changes in the cross section and thus varying stress states over the loading period. To take this effect into account, the creep strain increment $\Delta\boldsymbol{\varepsilon}_{\mathrm{cr},i}^{\mathrm{PS}}$ in the principal stress space is calculated element by element for each load spectrum according to Eq. (22). This represents the difference between the creep strains $\boldsymbol{\varepsilon}_{\mathrm{cr}}^{\mathrm{PS}}(t_i)$ and $\boldsymbol{\varepsilon}_{\mathrm{cr}}^{\mathrm{PS}}(t_{i-1})$ that the element would have experienced under the creep-relevant stress applied in the current load collective up to the current time t_i and the time before the current load collective t_{i-1}. The degraded modulus of elasticity E_i of the respective element is also taken into account. The calculated creep strains in the principal direction are transformed into the global *xyz*-coordinate system using Eq. (23) in the same way as the basic transformation described in Sect. 4.1. The creep strain increments $\Delta\boldsymbol{\varepsilon}_{\mathrm{cr},i}^{xyz}$ are then cumulated to the total viscous strain component $\boldsymbol{\varepsilon}_{\mathrm{cr}}^{xyz}$ of the element according to Eq. (24) and assigned to the element:

$$\Delta\boldsymbol{\varepsilon}_{\mathrm{cr},i}^{\mathrm{PS}} = \boldsymbol{\varepsilon}_{\mathrm{cr}}^{\mathrm{PS}}(t_i) - \boldsymbol{\varepsilon}_{\mathrm{cr}}^{\mathrm{PS}}(t_{i-1}) \tag{22}$$

$$\Delta\boldsymbol{\varepsilon}_{\mathrm{cr},i}^{xyz} = \boldsymbol{T}_i^{\mathrm{PS}\rightarrow xyz}\,\Delta\boldsymbol{\varepsilon}_{\mathrm{cr},i}^{\mathrm{PS}}\,\boldsymbol{T}_i^{\mathrm{PS}\rightarrow xyz\,\mathrm{T}} \tag{23}$$

$$\boldsymbol{\varepsilon}_{\mathrm{cr}}^{xyz} = \sum_{i=1}^{m} \Delta\boldsymbol{\varepsilon}_{\mathrm{cr},i}^{xyz} \tag{24}$$

4.3 Plastic Strain Component

The plastic strain component includes all irreversible concrete strains caused by fatigue loading. It can, therefore, be simplified as an incremental increase in strain per load cycle. This strain component can only be calculated from the measured total strain by determining the other strain components. The evaluation in von der Haar and Marx (2018) resulted in a linear correlation between the calculated plastic strain component and the logarithmic number of cycles to failure of each specimen, which was refined to Eq. (25) in Birkner and Marx (2019). Accordingly, when the number of cycles to failure N_f is reached, the concrete specimens exhibit a plastic strain $\varepsilon_d(N_f)$. It increased continuously with each load cycle during fatigue loading until this value was reached. However, this is only valid under the assumption of constant maximum and minimum stress:

$$\varepsilon_d(N_{\mathrm{f}}) = \left(-0.278959 \cdot \log N_{\mathrm{f}}\right) \cdot 10^{-3} \tag{25}$$

In beam tests, however, different stresses occur at the same location due to the expected degradation processes over the load duration, meaning that this relationship cannot be applied directly. For simplification, a linear increase in the plastic strains over the load cycles is assumed. With each load spectrum i in the iterative calculation process, a percentage $\Delta\boldsymbol{\varepsilon}_{d,i}^{\mathrm{PS}}$ of this total strain is accumulated. The magnitude depends on the relative fatigue life increment $\Delta\boldsymbol{\nu}_i^{\mathrm{PS}}$ from Sect. 4.1 according to Eq. (26). If the fatigue life increment is very small, which means that only few load cycles are part of the respective load spectrum, the plastic strains only increase by a small amount. In contrast, if the fatigue life increment has a value of 1.0, the plastic strain increases by the maximum possible value $\varepsilon_d(N_{\mathrm{f}})$. This means that all bearable load cycles are applied in the current load spectrum. The plastic strain increments are then transformed into the global coordinate system using the basic transformation in Eq. (27). The increments are accumulated over the load spectra to the plastic strain $\boldsymbol{\varepsilon}_d^{xyz}$ of the element according to Eq. (28):

$$\Delta\boldsymbol{\varepsilon}_{d,i}^{\mathrm{PS}} = \Delta\boldsymbol{\nu}_i^{\mathrm{PS}} \cdot \left(-0.278959 \cdot \begin{bmatrix} \lg N_{\mathrm{f},i}^{\mathrm{I}} \\ \lg N_{\mathrm{f},i}^{\mathrm{II}} \\ \lg N_{\mathrm{f},i}^{\mathrm{III}} \end{bmatrix}\right) \cdot 10^{-3} \tag{26}$$

$$\Delta\boldsymbol{\varepsilon}_{d,i}^{xyz} = \boldsymbol{T}_i^{\mathrm{PS}\rightarrow xyz}\,\Delta\boldsymbol{\varepsilon}_{d,i}^{\mathrm{PS}}\,\boldsymbol{T}_i^{\mathrm{PS}\rightarrow xyz\,\mathrm{T}} \tag{27}$$

$$\boldsymbol{\varepsilon}_d^{xyz} = \sum_{i=1}^{m} \Delta\boldsymbol{\varepsilon}_{d,i}^{xyz} \tag{28}$$

4.4 Temperature Strain Component

Based on the model in Bode and Marx (2021), concrete heating is assumed to be a result of the damage due to fatigue loading. For the calculation of the temperature strain component, a load cycle number-dependent heating is assumed for simplification. This was derived from results of fatigue tests on concrete cylinders (on average $D/H = 103$ mm/280 mm, $f_{\mathrm{c}} \approx 70$ N/mm^2) from von der Haar and Marx (2018). In this test series, load frequencies of 1 Hz and 10 Hz and maximum stress levels $S_{\max} = 0.80$, $S_{\max} = 0.70$ and $S_{\max} = 0.60$ were investigated. The minimum stress level was $S_{\min} = 0.05$ for all tests. Table 3 shows the resulting average heating rates, which

Table 3 Mean heating rates of the specimens in Kelvin/cycle, taken from the test series in von der Haar and Marx (2018)

$S_{\max}$	1 Hz	10 Hz
0.80	0.001325	0.001488
0.70	0.000085	0.000682
0.60	0.000017	0.000201

correspond to the heating divided by the respective number of cycles to failure.

In the experiments, the specimens tested at a loading frequency of 1 Hz at the maximum stress levels $S_{max}=0.70$ and $S_{max}=0.60$ did not heat up any further after a certain point. In the model, the heating rate is set to zero after this point for these boundary conditions. For the other experiments, in which the specimens heated up almost linearly until failure, the linear progression is further extrapolated for simplification. To prevent unrealistic temperatures with large numbers of load cycles, a limit of 80 °C is defined, which is based on experience from the literature, e.g., (Deutscher et al., 2020; Elsmeier & Lohaus, 2014; Otto et al., 2017).

In the numerical model, the temperature development is taken into account by increasing the element temperature. For this purpose, the heating rates from Table 3 are interpolated element by element with respect to the largest principal stress and the loading frequency and multiplied with the number of applied load cycles. The resulting heating is applied to all nodes of the element. The temperature strains are then determined according to Eq. (3). Temperature changes due to heat dissipation to the environment are neglected in the simulation, so that the strains are calculated directly from the applied temperature. This type of implementation greatly simplifies the heating behavior, as the ratio of cross-sectional area to surface area of the cylinders is significantly different from that of the beams. However, the focus of this work is not on the exact modeling of concrete heating and this simplification is, therefore, considered to be sufficiently accurate.

4.5 Solution Process in the Model

The numerical implementation of the extended additive strain model is done in an iterative calculation sequence. The load cycles are grouped into load spectra for simplification. Each load spectrum represents one iteration run. Within an iteration, the model is computed quasi-statically once with the loads of the minimum and once with those of the maximum stress level. The results are used in a subsequent evaluation algorithm that calculates the element damage and the individual strain components.

In the first load spectrum only a single load cycle is considered. This has proven to be useful, as local stress peaks can occur in the area of the load application, especially in the undamaged system. With only one load cycle, these cause only minor damage in the model, which ensures a reduction of stress peaks in all subsequent load spectra.

The evaluation algorithm uses the saved stresses of all elements from the calculation of the minimum and maximum stress level in a loop over all elements. In the loop, the maximum tolerable load cycles are first calculated based on the principal stresses. With them, the relative fatigue life increments in the principal directions are determined. After a transformation into the global coordinate system, they are used to calculate the relative fatigue life as a scalar value. With this, the new modulus of elasticity for each element is determined using the relative stiffness function.

A creep calculation determines the viscous strain component and the element temperature is calculated for the temperature strain component. The accumulated plastic strain component is determined using the relative fatigue life increment. The strain values are assigned to the elements via the INISTATE command and saved. This concludes the evaluation algorithm and a check is carried out whether a failure criterion has already been met. This can be, for example, the occurrence of excessive deformations. In this case, the calculation is finished. Otherwise, the element stiffnesses are adjusted, the new temperature boundary conditions are applied and the simulation

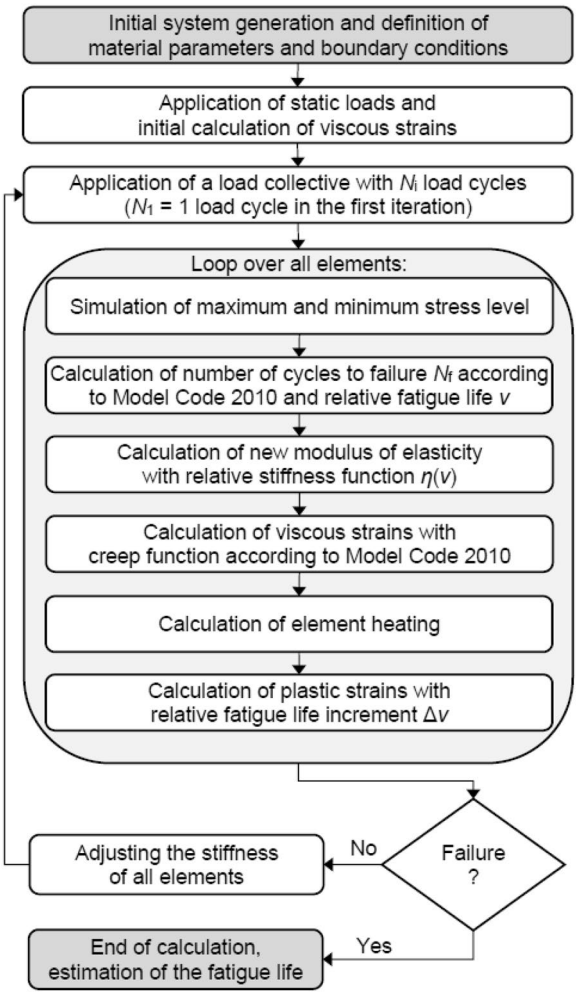

Fig. 6 Flowchart of the solution process

is continued with the next load spectrum. Fig. 6 shows a visualization of the solution process.

5 Numerical Model

SOLID226 solid elements with degrees of freedom for nodal displacements and temperatures were used to mesh the beam geometry in ANSYS Mechanical. The steel anchor plates at both ends of the beam were also meshed with this element type. The threaded rods for the horizontal prestressing force were realized with BEAM188-elements. Vertical degree of freedom constraints on nodes represented the two supports of the beam. In the experiments, longitudinal displacement of the beam was possible due to the roller bearings. A completely unrestricted freedom of movement is not reasonable in numerical models for stability reasons, so COMBIN14 spring elements were attached to the beam in this direction. Their spring stiffness was chosen to be very low, so that it had no influence on the results.

The vertical spring prestressing and the imbalance load were applied as quasi-static nodal forces to load application plates rigidly connected to the concrete elements. To apply the longitudinal prestressing, the beam elements of the rods were assigned prestressing sections and the force was applied. The beam elements themselves were rigidly coupled to the anchor plates at both ends of the beam. The magnitude of the applied forces was calculated from the boundary conditions measured in the experiments. For this purpose, the forces were averaged over the test duration and applied as constant values in the numerical model. In the experiments, the values showed only small deviations from the target value of mostly less than 4%, so this is considered to be sufficiently accurate.

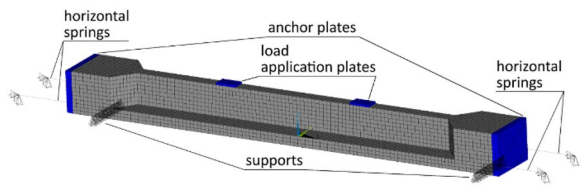

Fig. 7 Numerical model of the beam specimen, taken from Birkner and Marx (2021)

Fig. 7 shows the numerical model with the boundary conditions and Table 4 the applied forces and load cycles. The italic-highlighted beams did not show complete failure at the end of the tests. Beam C80–3 was the test beam for which no failure was targeted. It was, therefore, subjected to a higher minimum stress level and the test was ended after the correct functionality of the test facility had been ensured. Beam C40–1 only exhibited a few cracks in the most heavily stressed region and could have endured further load cycles, but the concrete was severely damaged below one load application point, which meant that constant imbalance excitation could no longer be maintained. Beam C40–2a showed no visible damage after almost 63.9 million load cycles, so the test was stopped at this point and continued at the higher load level under the name C40–2b.

6 Evaluation of the Experimental and Numerical Investigations

6.1 Failure Modes of the Beam Specimens

The beam specimens showed different damage states at the end of the tests. The end was defined when the imbalance force could not be further held constant.

Table 4 Load levels, frequencies, applied forces and number of load cycles of the beam specimens, averaged over the test duration

Beam specimen	S_{max}/S_{min}		Loading frequency in Hz	Longitudinal prestressing in kN	Spring prestressing per traverse beam in kN	Double force amplitude in kN	Number of load cycles
	Targeted	Realized					
C80-1	0.75/0.05	0.746/0.043	17.48	2317	117.8	518.9	97,325
C80-5		0.763/0.063	16.98	2359	112.5	477.3	73,497
C80-2	0.65/0.05	0.633/0.072	16.89	2330	105.0	398.4	1,551,912
C80-3[a]		*0.642/0.166*	*17.20*	*2176*	*100.3*	*305.2*	*2,321,824*
C80-4		0.654/0.091	16.93	2296	93.4	368.8	2,918,037
C40-1	0.75/0.05	*0.730/0.093*	*15.31*	*1418*	*46.7*	*205.8*	*3,664,615*
C40-2b[b]		0.745/0.084	14.61	1394	49.6	231.0	53,951
C40-4		0.736/0.088	15.49	1671	50.5	230.1	1,325,000
C40-2a	0.65/0.05	*0.629/0.081*	*14.94*	*1552*	*42.6*	*197.5*	*63,883,813*
C40-3[c]		–	–	–	–	–	–

[a] Test specimen

[b] Specimen with damage due to prior loading

[c] Damaged during installation

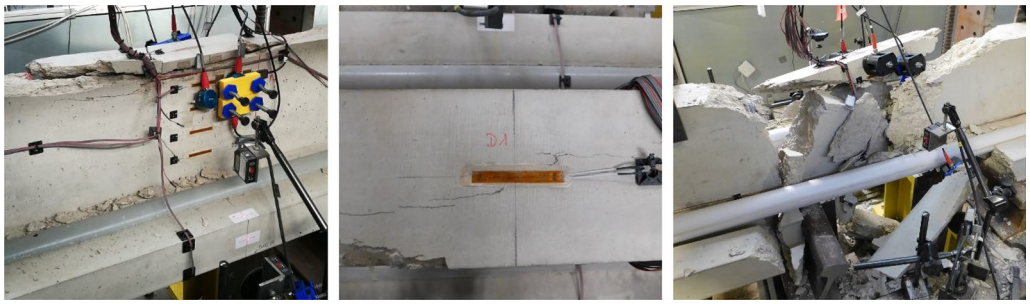

Fig. 8 Specimens after the tests: C80–1 (left), C80–4 (middle) and C40–2b (right), taken from Birkner and Marx (2022)

This was due to different reasons. In some cases, the beam specimens were completely destroyed, whereas others only showed small cracks. Fig. 8 gives three examples of different failure modes. In case of beam C80–4 there were larger cracks below one load application which did not allow further loading to be applied. In the other two examples, cracks in longitudinal direction formed in the upper compressive zone due to the fatigue loading. With further load cycles this led to concrete spalling at the upper edge of the cross section. In the case of beam C40–2b the test could not be stopped immediately and the rest of the cross section failed a few load cycles later.

6.2 Strain Development

The beam tests were simulated with the described boundary conditions and the results were compared with the measured data from the tests. For this, the numerical models were loaded with the same number of cycles which the specimens in the respective test had endured. Fig. 9a, b shows the strain curves of the beams at the maximum stress level at the top of the beam over the

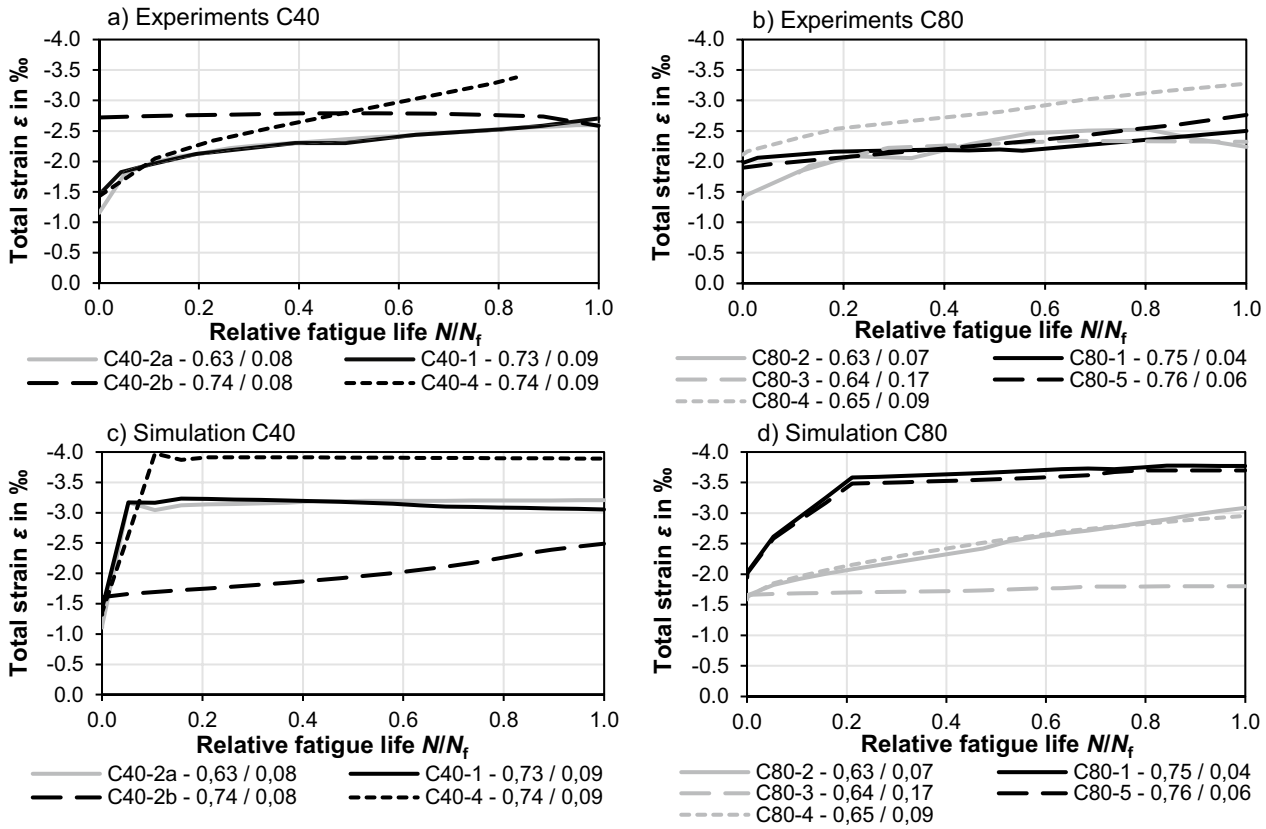

Fig. 9 Total strain at the top of the beams in the tests and numerical simulations

relative fatigue life N/N_f. For all beams, the greatest increase in strain occurred during the first 10% of the fatigue life. In this phase, cracking initiated by the fatigue loading had the greatest influence on the strains. After this phase, the crack initiation process was mostly completed and the beams entered a phase in which the concrete strains increased continuously. Most of the beams failed abruptly at the end, as evidenced by the lack of significant strain increase shortly before failure. The characteristic three-phase material behavior of concrete under fatigue loading observed in tests on cylindrical concrete specimens could not be determined in the beam tests.

The strain values of beam C40–2b at the start of the test were significantly higher than for the other beams because of the pre-existing damage caused by the loading at the lower stress level. As expected, they were as large as the final value of the previous test (beam C40–2a). There must have been many small invisible cracks around the strain gage at the top of the beam. As a result, the concrete in this area was slightly relieved and the strain even decreased with further load cycles.

Fig. 9c, d shows the strain curves of the beams from the simulations for comparison. At the beginning, the calculated strain values corresponded very well with the values measured in the tests. This confirms that the model reproduces the beam behavior in the undamaged state very well. As the number of load cycles increased, the strains in the numerical calculations for some beams increased significantly more than in the tests. This is particularly the case for the beams at the higher maximum stress level (black lines). In each case, the later maximum value of the strains was already reached after 10 or 20% of the relative fatigue life. The reason for this is that the respective element at the top of the beam was already completely damaged at this point and, therefore, could not sustain any further increase in strain. Further down in the cross section, however, the damage continued to progress. In the other simulations, the uppermost element did not reach the full degree of damage by the end of the calculation, so that the strains continued to increase with each load spectrum. At the end of the test, the strain values of the tests and simulations were between 2.5 and 3.5‰. It can, therefore, be concluded that the numerical model calculates the strains in a generally acceptable manner.

Figs. 10, 11, 12 show examples of the distributions of the elastic, plastic and viscous strain in beam C80–4 at the end of the simulation. The region at the upper edge of the cross section between the load application points shows the largest strains. Locally increased strain values can also be seen besides the load application points. These result from stress peaks caused by the concentrated load application. All three strain components decrease in magnitude from the middle of the beam downwards into the cross section.

6.3 Stiffness Development

Local stiffness changes can be observed element by element in the numerical model by means of the modulus of elasticity. This is shown in Fig. 13a, b in relation to the

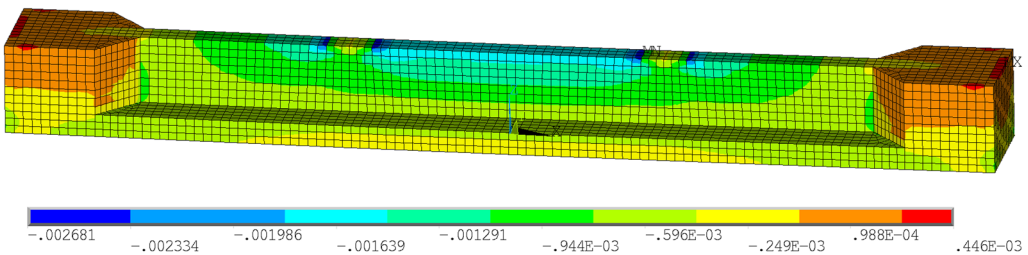

Fig. 10 Distribution of the elastic strain in normal direction in beam C80–4 at the end of the simulation

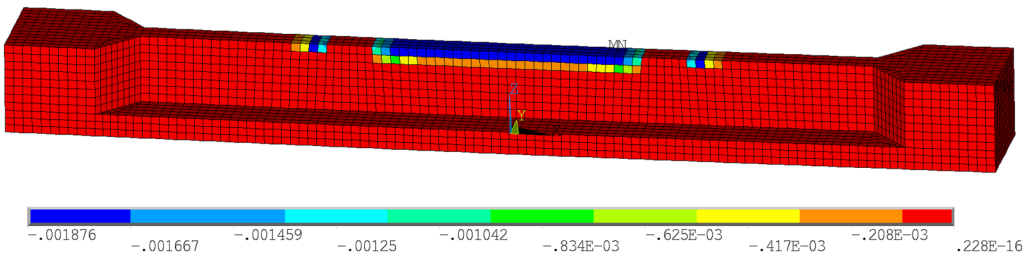

Fig. 11 Distribution of the plastic strain in normal direction in beam C80–4 at the end of the simulation

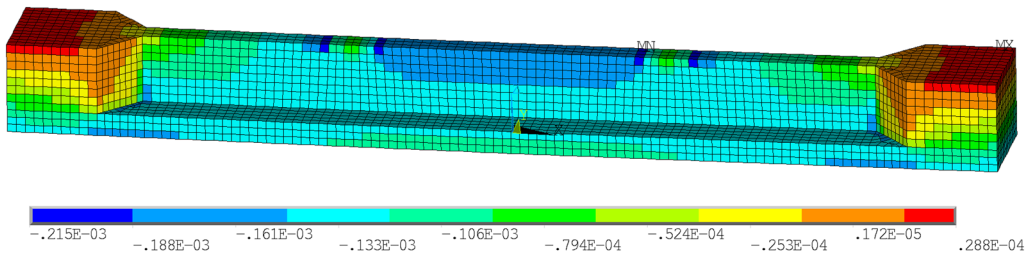

Fig. 12 Distribution of the viscous strain in normal direction in beam C80–4 at the end of the simulation

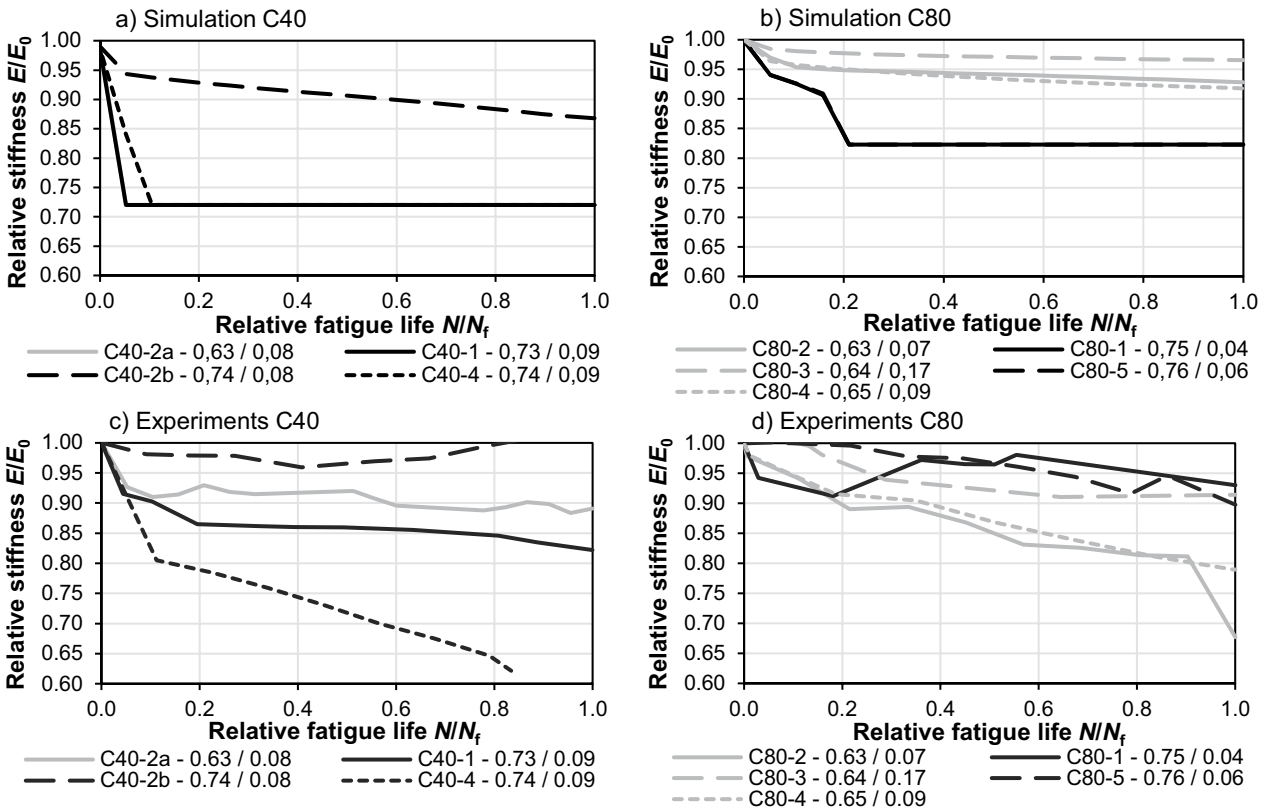

Fig. 13 Courses of the modulus of elasticity of the beams over the relative fatigue life in the tests and numerical simulations

respective initial value of the calculations over the relative fatigue life. The uppermost element in midspan is considered in all cases. Particularly the C80-beams, which were loaded at the higher maximum stress level, showed a significant early stiffness reduction, which already led to complete damage of the element during the first 20% of the fatigue life. In this case, the modulus of elasticity was set to the defined residual stiffness and was not changed from that point on. The other curves also show a stiffness drop at the beginning, but less significantly. Subsequently, the stiffness of these beams decreased continuously until the end of the calculation.

In the simulation of the C40-beams, complete damage occurred in all beams except C40–2b. This was the pre-damaged specimen, which had not failed after its planned loading at the lower maximum stress level. This pre-damage was not realized in the numerical model. This is why the simulated beam endured more load cycles than the specimen from the experiment.

Fig. 13c, d shows the curves of the relative modulus of elasticity from the experiments for comparison. These were calculated using the secant modulus between the maximum and minimum stress state of the measured strain and force values under the assumption of a

uniform stiffness distribution. The stiffness curves from the experiments scattered significantly more than in the numerical calculations. This is due to the spread of the concrete properties, whereas in the numerical model the averaged curve for the stiffness degradation was used for each concrete type. However, the final values of the relative modulus of elasticity agree well in general.

The beams showed the greatest stiffness reduction at the upper edge of the cross section. Further down in the cross section, it was significantly smaller both in the tests and in the numerical calculations. The fatigue damage was concentrated in the most heavily stressed region, which is well reproduced in the numerical calculation. This is also shown in Fig. 14, in which the distribution of the modulus of elasticity of beam C80–1 at the end of the calculation is compared to the damaged specimen after the test. The spalled concrete compression zone in the test corresponds very well to the most heavily damaged region in the numerical model. A detailed evaluation of the stiffness development of the beam specimens is described in Birkner et al. (2024).

6.4 Stress Redistribution

In contrast to the experiments, the actual stress in the cross section can be analyzed directly at any time in the numerical model. Fig. 15 shows the stress curves related to the respective initial values over the cross-sectional height at the end of the simulations for all models. For most of the beams, the stress at the upper edge of the cross section decreased over the loading period and increased in the interior of the cross section. For the models C80–1, C80–5 and C40–2b, however, the stresses at the upper edge of the cross section were higher at the end of the simulation than at the beginning. Further down in the cross section, in contrast, the stresses decreased. Only in model C40–2b they became greater again at the bottom edge. In the beam models C80–1 and C80–5, the stress at the top first decreased up to around 20% of the relative fatigue life and then increased again. This was the point at which the respective element was completely damaged.

In the other C80 models, only partial damage occurred at the upper edge of the cross section during the entire test duration. However, as there were only very small changes in stiffness (< 0.2%) in the bottom half of the cross section, it is assumed that the neutral fiber of the C80–1 and C80–5 models shifted successively more downwards as a result of damage than in the other models. The resulting change in the eccentricity of the longitudinal prestressing led to different strain and stress distributions. This secondary effect also caused stress redistributions in the cross section. It counteracted the stress reduction due to material degradation and resulted in an increase of stress at the top of the beam in midspan after the initial reduction up to about 20% of the fatigue life.

The model of beam C40–2b behaved differently at first glance. It is the only one of the C40 models that was not completely damaged at the upper edge at the end of the calculation. Nevertheless, comparable effects to the C80–1 and C80–5 models can also be found here.

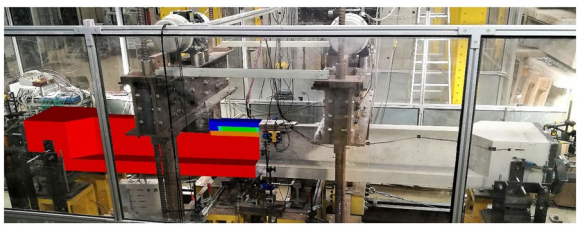

Fig. 14 Stiffness distribution of beam C80–1 at the end of the simulation compared to the damaged specimen from the test

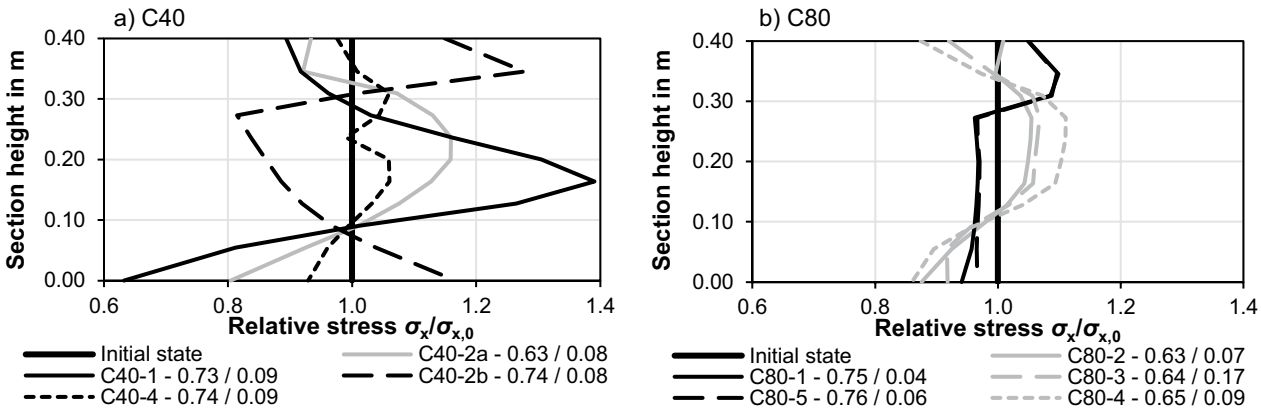

Fig. 15 Distribution of relative stress along the section heigt in midspan of the beams

The stiffness reduction further down in the cross section is comparatively low for this model too. Furthermore, the elastic strain at the upper edge of the cross section also increased continuously in model C40–2b, while the strains in the interior of the cross section actually decreased. This also indicates a shift of the neutral fiber compared to the other C40 models. The fact that no complete damage of an element occurred in this model is because the pre-damage caused by the previous loading at the lower maximum stress level was not taken into account in the numerical model and the calculation was stopped after the same number of load cycles as in the test. It can be concluded from this that this is not yet the state of failure and that the stress distribution would, therefore, still change if the calculation was continued.

7 Conclusion and Outlook

In this article, the additive strain model from von der Haar and Marx (2018) was extended and numerically implemented to simulate the strain and damage development of concrete subjected to fatigue loading. The concrete strains consist of four components: an elastic, a plastic, a viscous and a temperature strain component. The model can be used to investigate the influences of stress redistributions, like the ones that occur in wind turbine towers as a result of cyclic bending loads from the wind. The implementation was validated using large-scale fatigue tests on prestressed concrete beams. The following findings can be drawn from the investigations:

- The numerical simulations confirmed the effects observed in the beam tests. In particular, the most heavily damaged areas could be determined very well with the model.
- The strain development was generally well estimated with the numerical model for the region at the upper edge of the cross section in midspan. Here, the strain values of the tests and simulations were between 2.5 and 3.5‰. In particular, the plastic and viscous strains in this region were in good agreement with the test data.
- Stiffness reductions of up to 30% were found to occur at the top of the cross section in mid span of the beams.
- The model and the experimental validation proved the occurrence of stress redistribution in fatigue-loaded concrete components. At the upper edge of the cross section, there were stress reductions of up to 10% and at mid height stress increases of up to 40%. This confirmed the positive effect on the fatigue life of the components.

Since verifications against concrete fatigue in current design practice are predominantly based on the *S*–*N*-curves for centrically loaded concrete cylinders, these underestimate the actual tolerable number of load cycles of structures that are subjected to cyclic bending loads during their service life. This means that there is still potential to increase the cross-sectional efficiency. The model implemented in this work is, for example, suitable for carrying out parameter studies with varying load levels or degrees of prestress. This can already provide valuable insights for the pre-dimensioning of fatigue-loaded components and for the identification of critical regions in the geometry. For more detailed conclusions, additional tests have to be carried out to expand the numerical model to a wider range of parameters. At this state, the model can be applied to plain concrete only. To use the model to investigate the fatigue behavior of reinforced concrete beams, further investigations have to be carried out.

Acknowledgements
The authors would like to thank the funding bodies for the financial support and all project participants for their constructive cooperation.

Author contributions
The first author, DB, prepared the research plan, planned, supervised and evaluated the experimental investigations. DB also carried out the numerical implementation of the strain model and did the simulation and evaluation. SM provided the ressources, acquired the funding and supervised the experimental program. DB created the initial concept for the manuscript and prepared the original draft. SM supported the writing of the paper and provided the final review. All authors read and approved the final manuscript.

Funding
Open Access funding enabled and organized by Projekt DEAL. The underlying experimental investigations were part of the joint research project 'WinConFat' (Funding code: 0324016A) funded by the Federal Ministry for Economic Affairs and Climate Action (BMWK). The development of the numerical model was part of the research funded by Deutsche Forschungsgemeinschaft (DFG) in the research project 'Numerical and experimental investigations on stress redistributions of fatigue loaded concrete structures in the very high-cycle fatigue range' (Project number: 417209030).

Availability of data and materials
The data sets used during the current study are available from the corresponding author on reasonable request.

Declarations

Competing interests
The authors declare that they have no competing interests.

Received: 27 August 2024 Accepted: 9 January 2025
Published online: 24 March 2025

References

Abhijith, B. S., & Atul Narayan, S. P. (2023). Quantification of damage-related dissipation of asphalt concrete using the viscoelastic continuum damage framework. *Matériaux Et Constructions, 56*(8), 1–14. https://doi.org/10.1617/s11527-023-02241-6

Alliche, A. (2004). Damage model for fatigue loading of concrete. *International Journal of Fatigue, 26*(9), 915–921. https://doi.org/10.1016/j.ijfatigue.2004.02.006

Baktheer, A., Aguilar, M., & Chudoba, R. (2021). Microplane fatigue model MS1 for plain concrete under compression with damage evolution driven by cumulative inelastic shear strain. *International Journal of Plasticity, 143*, 102950. https://doi.org/10.1016/j.ijplas.2021.102950

Baktheer, A., & Chudoba, R. (2019). Classification and evaluation of phenomenological numerical models for concrete fatigue behavior under compression. *Construction and Building Materials, 221*, 661–677. https://doi.org/10.1016/j.conbuildmat.2019.06.022

Baktheer, A., Esfandiari, S., Aguilar, M., Becks, H., Classen, M., & Chudoba, R. (2024a). Fatigue-induced stress redistribution in prestressed concrete beams modeled using the constitutive hypothesis of inter-aggregate degradation. *Fatigue & Fracture of Engineering Materials & Structures*. https://doi.org/10.1111/ffe.14388

Baktheer, A., Goralski, C., Hegger, J., & Chudoba, R. (2024b). Stress configuration-based classification of current research on fatigue of reinforced and prestressed concrete. *Structural Concrete*. https://doi.org/10.1002/suco.202300667

Baktheer, A., Martínez-Pañeda, E., & Aldakheel, F. (2024c). Phase field cohesive zone modeling for fatigue crack propagation in quasi-brittle materials. *Computer Methods in Applied Mechanics and Engineering, 422*, 116834. https://doi.org/10.1016/j.cma.2024.116834

Becks, H., Aguilar, M., Chudoba, R., & Classen, M. (2022). Characterization of high-strength concrete under monotonic and fatigue mode II loading with actively controlled level of lateral compression. *Matériaux Et Constructions, 55*(10), 1–16. https://doi.org/10.1617/s11527-022-02087-4

Becks, H., Baktheer, A., Marx, S., Classen, M., Hegger, J., & Chudoba, R. (2023). Monitoring concept for the propagation of compressive fatigue in externally prestressed concrete beams using digital image correlation and fiber optic sensors. *Fatigue & Fracture of Engineering Materials & Structures, 46*(2), 514–526. https://doi.org/10.1111/ffe.13881

Betz, P., Curosu, V., Loehnert, S., Marx, S., & Curbach, M. (2023). Classification of multiaxial behaviour of fine-grained concrete for the calibration of a microplane plasticity model. *Buildings, 13*(11), 2704. https://doi.org/10.3390/buildings13112704

Birkner, D., Beltrán Gutiérrez, R. E., & Marx, S. (2024). Comparison of stiffness degradation in fatigue-loaded concrete cylinders and large-scale beams. *Engineering Structures, 302*, 117360. https://doi.org/10.1016/j.engstruct.2023.117360

Birkner, D., Freybe, N., & Marx, S. (2023). Bestimmung und Validierung von Materialparametern für die nichtlineare Modellierung von Beton. *Beton- und Stahlbetonbau, 119*(3), 190–199. https://doi.org/10.1002/best.202300081

Birkner, D., & Marx, S. (2019). Spannungsumlagerungen bei ermüdungsbeanspruchten Spannbetonbalken im numerischen Modell und Versuch. *Beton- und Stahlbetonbau, 114*(8), 575–583. https://doi.org/10.1002/best.201900026

Birkner, D., & Marx, S. (2021). Large-scale fatigue tests on prestressed concrete beams. In A. Abu (Chair), *IABSE Congress 2020 Proceedings: Resilient technologies for sustainable infrastructure,* Christchurch, New Zealand.

Birkner, D., & Marx, S. (2022). Stiffness degradation in fatigue loaded large concrete beams. In S. Stokkeland & H. C. Braarud (Chairs), *Concrete Innovation for Sustainability: Proceedings for the 6th fib International Congress 2022,* Oslo, Norway.

Bode, M., & Marx, S. (2019). Heat generation during fatigue tests on concrete specimens. In W. Derkowski, P. Gwozdziewicz, L. Hojdys, P. Krajewski, & M. Pantak (Chairs), *Concrete Innovations in Materials, Design and Structures: Proceedings of the 16th fib Symposium,* Krakow, Poland.

Bode, M., & Marx, S. (2021). Energetic damage analysis regarding the fatigue of concrete. *Structural Concrete, 22*(S1), E851–E859. https://doi.org/10.1002/suco.202000416

Bögl, S., Gläser, C., & Traute, M. (2013). Vorgespannte Hybridtürme für Windenergieanlagen. *Bauingenieur, 88*(7), 301–306.

Carpinteri, A., Spagnoli, A., & Vantadori, S. (2005). Mechanical damage of ordinary or prestressed reinforced concrete beams under cyclic bending. *Engineering Fracture Mechanics, 72*(9), 1313–1328. https://doi.org/10.1016/j.engfracmech.2004.10.005

de Monteiro, V. M. A., Cardoso, D. C. T., & de Andrade Silva, F. (2024). On the mechanical degradation of R/SFRC beams under flexural fatigue loading. *Matériaux Et Constructions, 57*(4), 1–18. https://doi.org/10.1617/s11527-024-02371-5

Desmorat, R., Ragueneau, F., & Pham, H. (2007). Continuum damage mechanics for hysteresis and fatigue of quasi-brittle materials and structures. *International Journal for Numerical and Analytical Methods in Geomechanics, 31*(2), 307–329. https://doi.org/10.1002/nag.532

Deutscher, M., Tran, N. L., & Scheerer, S. (2020). Experimental investigations on temperature generation and release of ultra-high performance concrete during fatigue tests. *Applied Sciences, 10*(17), 5845. https://doi.org/10.3390/app10175845

Elsmeier, K., & Lohaus, L. (2014). Temperature development of concrete due to fatigue loading. In J. Bastien, N. Rouleau, M. Fiset, & M. Thomassin (Chairs), *Proceedings of The 10th fib International PhD Symposium in Civil Engineering,* Quebec, Canada.

fib. (2013). *fib model code for concrete structures 2010*. Ernst & Sohn. https://doi.org/10.1002/9783433604090

Fürll, F., Klein, F., Hartwig, S., Kang, C., Betz, T., & Marx, S. (2024). Experimental and analytical study on the load-bearing capacity of segmented tower structures with dry joints under combined loading. *Structural Concrete*. https://doi.org/10.1002/suco.202300873

Grünberg, J., Göhlmann, J., & Marx, S. (2014). Mechanische Modelle für mehraxiales Festigkeits- und Ermüdungsversagen von Stahlbeton. *Beton- und Stahlbetonbau, 109*(6), 403–416. https://doi.org/10.1002/best.201400022

Kern, B., Podhajecky, A.-L., Lohaus, L., Haist, M., & Oneschkow, N. (2024). Deformation behaviour of concrete with different moisture contents subjected to compressive creep and cyclic loading. *Matériaux Et Constructions, 57*(6), 1–17. https://doi.org/10.1617/s11527-024-02399-7

Kindrachuk, V. M., Thiele, M., & Unger, J. F. (2015). Constitutive modeling of creep-fatigue interaction for normal strength concrete under compression. *International Journal of Fatigue, 78*, 81–94. https://doi.org/10.1016/j.ijfatigue.2015.03.026

Kirane, K., & Bažant, Z. P. (2015). Microplane damage model for fatigue of quasibrittle materials: Sub-critical crack growth, lifetime and residual strength. *International Journal of Fatigue, 70*, 93–105. https://doi.org/10.1016/j.ijfatigue.2014.08.012

Klein, F., & Marx, S. (2021). Torsional load-bearing capacity of half-shell segments for prestressed concrete towers. *Engineering Structures, 243*, 112589. https://doi.org/10.1016/j.engstruct.2021.112589

Krüger, C., Curoşu, V., & Löhnert, S. (2024). An extended phase-field approach for the efficient simulation of fatigue fracture processes. *International Journal for Numerical Methods in Engineering, 125*(7), e7422. https://doi.org/10.1002/nme.7422

Liang, G.-Q., Chen, X., Jiang, B.-Y., & Jiang, C.-S. (2023). Fatigue life prediction of concrete under cyclic compression based on gradient boosting regression tree. *Matériaux Et Constructions, 56*(9), 1–19. https://doi.org/10.1617/s11527-023-02262-1

Mai, S. H., Le-Corre, F., Forêt, G., & Nedjar, B. (2012). A continuum damage modeling of quasi-static fatigue strength of plain concrete. *International Journal of Fatigue, 37*, 79–85. https://doi.org/10.1016/j.ijfatigue.2011.10.006

Makhlouf, M. H., El-Azab, I. A., & Mansour, M. H. (2024). Flexural improvement of RC slabs by FRP or steel using different strengthening systems and novel anchoring techniques. *International Journal of Concrete Structures and Materials, 18*(1), 1–28. https://doi.org/10.1186/s40069-024-00683-y

Otto, C., Elsmeier, K., & Lohaus, L. (2017). Temperature effects on the fatigue resistance of high-strength-concrete and high-strength-grout. In D. A. Hordijk & M. Lukovic (Chairs), *High Tech Concrete: Where Technology and Engineering Meet: Proceedings of the 2017 fib Symposium,* Maastricht, The Netherlands.

Pfanner, D. (2003). *Zur Degradation von Stahlbetonbauteilen unter Ermüdungsbeanspruchung*. Dissertation. *Fortschritt-Berichte VDI: Reihe 4, Nr. 189*. VDI-Verlag.

Schneider, S., Herrmann, R., & Marx, S. (2018). Development of a resonant fatigue testing facility for large-scale beams in bending. *International Journal of Fatigue, 113*, 171–183. https://doi.org/10.1016/j.ijfatigue.2018.03.036

Schramm, C., Birkner, D., & Marx, S. (2024). Resonance-based testing facility for fatigue tests of different axially loaded structural elements. *Engineering Structures, 298*, 117045. https://doi.org/10.1016/j.engstruct.2023.117045

von der Haar, C., & Marx, S. (2018). A strain model for fatigue-loaded concrete. *Structural Concrete, 19*(2), 463–471. https://doi.org/10.1002/suco.201700029

Wu, X., Zhang, X., Bhattarai, H. B., Hwang, H.-J., Yang, J., & Kang, S. (2022). Structural behavior analysis of UHPC hybrid tower for 3-MW Super tall wind turbine under rated wind Load. *International Journal of Concrete Structures and Materials, 16*(1), 1–13. https://doi.org/10.1186/s40069-022-00542-8

Zanuy, C., Albajar, L., & de la Fuente, P. (2009). Sectional analysis of concrete structures under fatigue loading. *ACI Structural Journal, 106*(5), 667–677. https://doi.org/10.14359/51663107

Publisher's Note

Dennis Birkner is Senior Engineer at Ramboll Deutschland GmbH, Lister Str. 9, 30163 Hannover, Germany.

Steffen Marx is director of the Institute of Concrete Structures and professor of DB Netz AG—Endowed Chair of Civil Engineering of Dresden University of Technology, 01062 Dresden, Germany.